

RIS-Assisted Quasi-Static Broad Coverage for Wideband mmWave Massive MIMO Systems

Muxin He, Jindan Xu, Wei Xu, *Senior Member, IEEE*, Hong Shen, Ning Wang,
and Chunming Zhao

Abstract

Reconfigurable intelligent surfaces (RISs) can establish favorable wireless environments to combat the severe attenuation and blockages in millimeter-wave (mmWave) bands. However, to achieve the optimal enhancement of performance, the instantaneous channel state information (CSI) needs to be estimated at the cost of a large overhead that scales with the number of RIS elements and the number of users. In this paper, we design a quasi-static broad coverage at the RIS with the reduced overhead based on the statistical CSI. We propose a design framework to synthesize the power pattern reflected by the RIS that meets the customized requirements of broad coverage. For the communication of broadcast channels, we generalize the broad coverage of the single transmit stream to the scenario of multiple streams. Moreover, we employ the quasi-static broad coverage for a multiuser orthogonal frequency division multiplexing access (OFDMA) system, and derive the analytical expression of the downlink rate, which is proved to increase logarithmically with the power gain reflected by the RIS. By taking into account the overhead of channel estimation, the proposed quasi-static broad coverage even outperforms the design method that optimizes the RIS phases using the instantaneous CSI. Numerical simulations are conducted to verify these observations.

Index Terms

Broad coverage, massive multiple-input multiple-output (MIMO), millimeter-wave (mmWave), orthogonal frequency division multiplexing (OFDM), quasi-static, reconfigurable intelligent surface (RIS).

M. He, J. Xu, W. Xu, H. Shen, and C. Zhao are with the National Mobile Communications Research Laboratory, Southeast University, Nanjing 210096, China (e-mail: mxhe@outlook.com; jdxu@seu.edu.cn; wxu@seu.edu.cn; shhseu@seu.edu.cn; cmzhao@seu.edu.cn). W. Xu is also with Henan Joint International Research Laboratory of Intelligent Networking and Data Analysis, Zhengzhou University, Zhengzhou 450001, China. C. Zhao is also with the Purple Mountain Laboratories, Nanjing, China.

N. Wang is with the School of Information Engineering, Zhengzhou University, Zhengzhou 450001, China (ienwang@zzu.edu.cn).

This work has been submitted to the IEEE for possible publication. Copyright may be transferred without notice, after which this version may no longer be accessible.

I. INTRODUCTION

Reconfigurable intelligent surfaces (RISs) are an innovative technology for implementing both spectral- and energy-efficient wireless networks beyond 5G [1]–[7]. It is well compatible with existing multi-antenna systems by mounting additional planar surfaces on the exterior walls of buildings. Each reflecting element independently changes the phase of the impinging signal such that an RIS is able to control the wireless environment. Empowered by this ability, RISs can improve the received signal power and can create optimized alternative propagation paths to bypass obstacles.

In millimeter-wave (mmWave) band, the wireless channel is vulnerable to the attenuation and blockages, which seriously affects the quality of service. RISs are, therefore, a promising technology for making mmWave communications more reliable [1], [2], [8], [9]. In [10], the authors studied the cooperative reflection design for multiple RISs under the mmWave channels by taking the timing synchronization errors into account. The authors of [11] designed the RIS to improve the channel capacity of a mmWave indoor environment without any line-of-sight (LoS) path. In [12], the authors maximized the spectral efficiency of an RIS-assisted mmWave system by exploiting the inherence structure of the cascaded mmWave channel. The authors of [13] estimated the cascaded channel for an RIS-assisted mmWave system with the quantized beamforming at the receiver. In [14], the authors jointly designed the hybrid precoding at the base station (BS) and the phase shifts of the RIS in a multiuser mmWave system.

Regarding mmWave systems with wide band, the orthogonal frequency division multiplexing (OFDM) is commonly applied to combat the frequency-selective fading. However, the RIS design method proposed for the single-carrier system cannot be directly employed to the OFDM based multi-carrier system since an RIS cannot provide independent phase control for each subcarrier. In [15], the authors maximized the achievable rate of an OFDM system by jointly optimizing the power allocation and the phase shifts of the RIS. The authors of [16] optimized the channel capacity of RIS-assisted OFDM systems by jointly designing the transmit covariance matrix and the phase shifts of the RIS. In [17], the authors improved the performance of an OFDM system with a low-complexity method that matches the phase shifts of the RIS with the phase of the strongest channel path. Considering the practical RIS model with dual phase- and amplitude-squint effect, the authors of [18] studied the sum-rate maximization problem for a multiuser multi-antenna OFDM system with continuous and discrete phase shifts at the RIS.

Furthermore, the reflection design of RISs relies on the channel state information (CSI) among the BS, the RIS, and the user equipment (UE), which is difficult to acquire due to the nearly-passive hardware and the limited sensing capability of RISs [1], [2]. Even worse, the overhead of channel estimation is huge since a large number of reflecting elements are equipped at the RIS in order to compensate for the path losses of the BS-RIS channel and the RIS-UE channel [19]. Accordingly, the authors of [15] and [17] utilized a grouping method to reduce the training overhead for RIS-assisted OFDM systems, where the adjacent RIS reflecting elements were grouped to share a common reflection coefficient. However, the channel estimation schemes proposed in [15] and [17] cannot be efficiently applied to the scenario of multiple users since the UE-by-UE successive channel estimation leads to a large overhead that scales with the number of users. In [20], the authors proposed two channel estimation schemes for the RIS-assisted multiuser orthogonal frequency division multiplexing access (OFDMA) system, where the maximum number of supported users was proved to be limited, and an increment of users was obtained at the expense of higher complexity and degraded performance. It was shown in [15], [17], and [20] that the large overhead of training and feedback poses a challenge for RIS-assisted OFDM systems.

Since the acquisition of full CSI is challenging with low-cost RIS circuits, some studies, e.g., [21]–[23], investigated RIS-assisted communications with partial CSI. Authors of [21] discussed a tradeoff between the energy efficiency and the spectral efficiency of an RIS-assisted multiuser multi-antenna system by using the partial CSI between the RIS and the users. In [22], with the CSI of signal-to-noise-ratio (SNR), the authors proposed an RIS-assisted opportunistic beamforming for broadcast channels. In a multi-antenna system assisted by multiple distributed RISs, the authors of [23] proposed a low-complexity RIS design by exploiting the statistical correlation information of channels.

In addition, in the communication of broadcast channels, not all the users' CSI are available. Therefore, the transmit signals are commonly precoded into a broad beam to cover the users at different locations, where the flat-top pattern with small power fluctuations is preferred. In conventional massive multiple-input multiple-output (MIMO) systems, the authors of [24] utilized the Zadoff-Chu sequence to design a channel-independent omnidirectional precoding that maintained the equal average radiation power in each spatial direction. In [25], the authors proposed the channel-independent omnidirectional space-time block coding to satisfy a more strict constant power constraint at any instant time. To obtain a flexible sector size of coverage,

the authors of [26] utilized the manifold optimization to synthesize the target flat-top pattern with negligible power fluctuations, which needed no CSI of users.

Considering the above difficulties in acquiring the CSI for the RIS design, the RIS-assisted broad coverage can be developed by broadening the power pattern reflected by the RIS. In [27], the authors employed the quadratic gradient phase shifts at the RIS instead of the linear gradient phase shifts to broaden the power pattern reflected by the RIS. However, the control of the power fluctuations within the broad beam was not mentioned. Other methods of beam broadening include the deactivation based technique and sub-array based technique [28]. The deactivation based technique generates a wider beam by turning off part of the antennas in an array, which, however, limits the maximal total transmit power when the number of active antennas is small [28]. The sub-array based technique points the beam of each sub-array towards a separated angle, and combines the multiple beams of the sub-arrays into a broad beam. In [29], the authors proposed a sub-array based beam broadening and flattening technique to the design of RIS phase shifts, which achieved better performance than the deactivation based method. However, the power pattern generated by [29] cannot admit a continuous adjustment of the beamwidth due to the limited spatial resolution of the sub-arrays, especially for a relatively small array. In [30], inspired by [26], we adopted the manifold method to synthesize a customized flat-top power pattern with an arbitrarily defined beamwidth at the RIS. Since the non-convex constant modulus constraint on the phase shift is a challenge of the RIS design, we can regard this constraint as a manifold to facilitate the optimization [31].

Note that the above beam broadening techniques relies on the single incident angle of arrival at the RIS, e.g., the LoS channel path. However, in the RIS-assisted communication of broadcast channels, the transmission design using the LoS BS-RIS channel results in an equivalent rank-1 cascaded BS-RIS-UE channel, which hinders the transmission of multiple streams. Moreover, when the multi-stream transmission is supported by multiple channel paths between the BS and the RIS, the design method based on the LoS BS-RIS channel, e.g., as proposed in [29] and [30], cannot ensure a small power fluctuation within the coverage due to the interference from the non-LoS (NLoS) BS-RIS channel paths.

To address the aforementioned issues, we design the quasi-static broad coverage at the RIS by using the statistical CSI to reduce the overhead. Moreover, we utilize multiple mmWave BS-RIS channel paths in the pattern synthesis such that the rank of the cascaded channel matrix can support the transmission of multiple streams. Under the proposed quasi-static broad coverage,

we analyze the system performance in both the broadcast channel and the OFDMA channel. The main contributions of our work are summarized as follows.

1) We propose a design framework to synthesize the flat-top power pattern reflected by the RIS in a mmWave massive MIMO-OFDM system, where the precoder at the BS and the phase shifts of the RIS are jointly designed. We regard the constant modulus constraint of the RIS phase shifts as a Riemannian manifold such that we can perform the conjugate gradient (CG) method to minimize the distance between the target pattern and the power pattern reflected by the RIS. The proposed design framework is general since it can be applied to the synthesis of a customized target pattern and to the scenario of multipath channel models. With the proposed design framework, we can provide a quasi-static broad coverage for the users by exploiting only the statistical CSI of mmWave channel paths, which saves the overhead of channel estimation and feedback.

2) In the communication of broadcast channels, we generalize RIS-assisted broad coverage of the single transmit stream to the scenario of multiple transmit streams. When the BS-RIS channel is simplified as an LoS channel to formulate the reflected flat-top pattern, the equivalent cascaded BS-RIS-UE channel is rank-1 and thus supports only a single transmit stream. In this paper, we employ a more general multipath mmWave model for the BS-RIS channel, which poses new challenge to the pattern synthesis. Therefore, multiple transmit streams can be supported by the equivalent high-rank cascaded BS-RIS-UE channel, which, to the best of our knowledge, has not been provided in the literature. Moreover, it is proved that, within the broad coverage, each user receives a constant average received power.

3) In order to provide reliable communications for multiuser OFDMA systems, we design a quasi-static flat-top power pattern at the RIS to cover the users instead of optimizing the RIS phase shifts with the instantaneous CSI. By using the dominant LoS channel, the proposed quasi-static broad coverage needs no more channel estimation for controlling the RIS, whose overhead approaches that of the conventional OFDMA system. Therefore, by taking the overhead into consideration, the proposed broad coverage even outperforms the RIS design method that needs the estimation of the instantaneous CSI. Furthermore, we derive an analytical expression of the downlink rate of the considered OFDMA system, and find that the rate increases logarithmically with the power gain reflected by the RIS.

The rest of this paper is organized as follows. Firstly, the considered system model is introduced in Section II. The manifold optimization is presented in Section III. In Section IV,

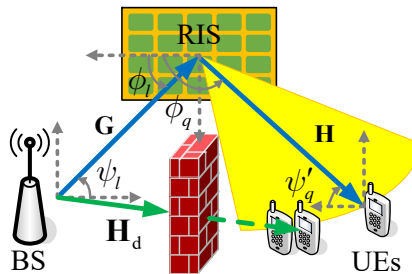


Fig. 1. RIS-assisted quasi-static broad coverage in a mmWave massive MIMO system.

we discuss the applications of broad coverage and analyze the system performance. Finally, simulations are conducted in Section V, and conclusions are drawn in Section VI.

Notation: Lowercase and uppercase boldface letters represent column vectors and matrices, respectively. \mathbf{A}^* , \mathbf{A}^T , and \mathbf{A}^H denote the conjugate, the transpose, and the Hermitian transpose of matrix \mathbf{A} , respectively. $\text{diag}(\mathbf{a})$ is the diagonal matrix with vector \mathbf{a} as its diagonal entries, and $\text{diag}(\mathbf{A})$ takes only the diagonal entries of matrix \mathbf{A} . $\text{vec}\{\cdot\}$ denotes the vectorization operator that stacks the columns of the input matrix into a long column. $\|\cdot\|_2$ and $\|\cdot\|_F$ denote the 2-norm and the Frobenius norm, respectively. $\text{tr}(\mathbf{A})$ denotes the trace of matrix \mathbf{A} . $\Re[\cdot]$ denotes the real part of the input. \circ denotes the Hadamard product. j denotes the imaginary unit. $\mathbb{C}^{m \times n}$ stands for the set of $m \times n$ complex matrices. \mathbb{Z} , \mathbb{R}^+ , and \emptyset denote the integer set, the set of positive real number, and the empty set, respectively.

II. SYSTEM MODEL

A. Signal Model

As shown in Fig. 1, we consider the RIS-assisted broad coverage in a mmWave massive MIMO system, where several users with N_{UE} antennas are served by a BS with N_{BS} antennas and assisted by an RIS with M reflecting elements. In the considered system, the BS fails to provide reliable communications for the users due to the obstacle between them, and an RIS is deployed around the obstacle to provide a broad coverage for the blocked users. For an OFDM-based downlink transmission, the received signal $\mathbf{r}[k] \in \mathbb{C}^{N_{\text{UE}} \times 1}$, at the k -th subcarrier, of one given user is

$$\mathbf{r}[k] = \sqrt{p} \left(\sqrt{\beta_1 \beta_2} \mathbf{H}[k] \mathbf{\Theta} \mathbf{G}[k] + \sqrt{\beta} \mathbf{H}_d[k] \right) \mathbf{W}[k] \mathbf{s}[k] + \mathbf{z}[k], \quad (1)$$

where p is the transmit power of the BS, β_1 , β_2 , and β are the large-scale fading factors of the BS-RIS channel, the RIS-UE channel, and the BS-UE direct channel, respectively, $\mathbf{H}[k] \in \mathbb{C}^{N_{\text{UE}} \times M}$

is the channel from the RIS to the user, $\Theta = \text{diag}(\theta_0, \theta_1, \dots, \theta_{M-1})$ is the phase matrix at the RIS, $\mathbf{G}[k] \in \mathbb{C}^{M \times N_{\text{BS}}}$ is the channel from the BS to the RIS, $\mathbf{H}_d[k] \in \mathbb{C}^{N_{\text{UE}} \times N_{\text{BS}}}$ is the direct channel from the BS to the user, $\mathbf{W}[k] \in \mathbb{C}^{N_{\text{BS}} \times N_d}$ is the precoding matrix of N_d transmit streams at the BS, $\mathbf{s}[k] \in \mathbb{C}^{N_d \times 1}$ is the transmit signal with $\mathbb{E}\{\mathbf{s}[k]\mathbf{s}^H[k]\} = \mathbf{I}_{N_d}$, and $\mathbf{z}[k] \in \mathbb{C}^{N_{\text{UE}} \times 1}$ is the additive white Gaussian noise (AWGN) following $\mathcal{CN}(\mathbf{0}, \sigma_z^2 \mathbf{I}_{N_{\text{UE}}})$. Note that the precoding matrices at N_c subcarriers are normalized to $\sum_{k=0}^{N_c-1} \|\mathbf{W}[k]\|_F^2 = N_c$.

B. Channel Model

As for the time-domain multipath mmWave channels $\mathbf{G}[n]$, $\mathbf{H}[n]$, and $\mathbf{H}_d[n]$, we adopt the geometric channel model as follows [32], [33]

$$\mathbf{G}[n] \triangleq \sqrt{N_{\text{BS}}M} \sum_{l=0}^{L-1} \alpha_l \mathbf{a}_{\mathbf{G}}(\phi_l) \mathbf{b}_{\mathbf{G}}^H(\psi_l) g(nT - \tau_l), \quad (2)$$

$$\mathbf{H}[n] \triangleq \sqrt{N_{\text{UE}}M} \sum_{q=0}^{Q-1} \alpha_q \mathbf{b}_{\mathbf{H}}(\psi'_q) \mathbf{a}_{\mathbf{H}}^H(\phi_q) g(nT - \tau_q), \quad (3)$$

$$\mathbf{H}_d[n] \triangleq \sqrt{N_{\text{BS}}N_{\text{UE}}} \sum_{q'=0}^{Q'-1} \alpha_{q'} \mathbf{b}_{\mathbf{H}}(\psi'_{q'}) \mathbf{b}_{\mathbf{G}}^H(\psi_{q'}) g(nT - \tau_{q'}), \quad (4)$$

where n is the sampling index, L , Q , and Q' are the numbers of paths of the BS-RIS channel, the RIS-UE channel, and the BS-UE direct channel, respectively, α_l , α_q , and $\alpha_{q'}$ are the complex gains of the l -th path of $\mathbf{G}[n]$, the q -th path of $\mathbf{H}[n]$, and the q' -th path of $\mathbf{H}_d[n]$, respectively, ϕ_l and ϕ_q are the angles of arrival (AoAs) of the l -th path of $\mathbf{G}[n]$ and the angles of departure (AoDs) of the q -th path of $\mathbf{H}[n]$, respectively, ψ_l and $\psi_{q'}$ are the AoDs of the l -th path of $\mathbf{G}[n]$ and the q' -th path of $\mathbf{H}_d[n]$, respectively, ψ'_q and $\psi'_{q'}$ are the AoAs of the q -th path of $\mathbf{H}[n]$ and the q' -th path of $\mathbf{H}_d[n]$, respectively, $\mathbf{a}_{\mathbf{G}} \in \mathbb{C}^{M \times 1}$ and $\mathbf{a}_{\mathbf{H}} \in \mathbb{C}^{M \times 1}$ are the array response vectors (ARVs) at the RIS that correspond to the signal arrival and the signal departure, respectively, $\mathbf{b}_{\mathbf{G}} \in \mathbb{C}^{N_{\text{BS}} \times 1}$ and $\mathbf{b}_{\mathbf{H}} \in \mathbb{C}^{N_{\text{UE}} \times 1}$ are the ARVs at the BS and the user, respectively, T is the sampling period, τ_l , τ_q , and $\tau_{q'}$ are the transmission delays of the l -th path of $\mathbf{G}[n]$, the q -th path of $\mathbf{H}[n]$, and the q' -th path of $\mathbf{H}_d[n]$, respectively, and $g(t)$ is the rectangular pulse shaping filter, i.e., $g(t) = 1$ only for $-T \leq t < 0$. Moreover, we assume that the channel paths undergo uncorrelated fading. Since a planar array can be treated as two decoupled linear arrays in the

pattern synthesis [29], in this paper, we use the model of uniform linear array at the BS, the RIS, and the UE for simplification and define the ARVs as follows

$$\mathbf{a}_{\mathbf{G}}(\phi_l) \triangleq \frac{1}{\sqrt{M}} \left[1, e^{-j\frac{2\pi}{\lambda}\rho \cos \phi_l}, \dots, e^{-j\frac{2\pi}{\lambda}(M-1)\rho \cos \phi_l} \right]^T, \quad (5)$$

$$\mathbf{b}_{\mathbf{G}}(\psi_l) \triangleq \frac{1}{\sqrt{N_{\text{BS}}}} \left[1, e^{-j\frac{2\pi}{\lambda}\rho \sin \psi_l}, \dots, e^{-j\frac{2\pi}{\lambda}(N_{\text{BS}}-1)\rho \sin \psi_l} \right]^T, \quad (6)$$

$$\mathbf{a}_{\mathbf{H}}(\phi_q) \triangleq \frac{1}{\sqrt{M}} \left[1, e^{j\frac{2\pi}{\lambda}\rho \cos \phi_q}, \dots, e^{j\frac{2\pi}{\lambda}(M-1)\rho \cos \phi_q} \right]^T, \quad (7)$$

$$\mathbf{b}_{\mathbf{H}}(\psi'_q) \triangleq \frac{1}{\sqrt{N_{\text{UE}}}} \left[1, e^{-j\frac{2\pi}{\lambda}\rho \sin \psi'_q}, \dots, e^{-j\frac{2\pi}{\lambda}(N_{\text{UE}}-1)\rho \sin \psi'_q} \right]^T, \quad (8)$$

where λ is the wavelength and $\rho = \lambda/2$ is the distance between adjacent elements.

As for the frequency-domain channels, we apply an N_c -dimensional discrete Fourier transform (DFT) to (2)-(4), and obtain

$$\mathbf{G}[k] = \sum_{n=0}^{N_c-1} \mathbf{G}[n] e^{-j\frac{2\pi kn}{N_c}} \triangleq \sqrt{N_{\text{BS}}M} \sum_{l=0}^{L-1} \delta_l[k] \mathbf{a}_{\mathbf{G}}(\phi_l) \mathbf{b}_{\mathbf{G}}^H(\psi_l), \quad (9)$$

$$\mathbf{H}[k] = \sum_{n=0}^{N_c-1} \mathbf{H}[n] e^{-j\frac{2\pi kn}{N_c}} \triangleq \sqrt{N_{\text{UE}}M} \sum_{q=0}^{Q-1} \delta_q[k] \mathbf{b}_{\mathbf{H}}(\psi'_q) \mathbf{a}_{\mathbf{H}}^H(\phi_q), \quad (10)$$

$$\mathbf{H}_d[k] = \sum_{n=0}^{N_c-1} \mathbf{H}_d[n] e^{-j\frac{2\pi kn}{N_c}} \triangleq \sqrt{N_{\text{BS}}N_{\text{UE}}} \sum_{q'=0}^{Q'-1} \delta_{q'}[k] \mathbf{b}_{\mathbf{H}}(\psi'_{q'}) \mathbf{b}_{\mathbf{G}}^H(\psi_{q'}), \quad (11)$$

where $\delta_l[k] \triangleq \sum_{n=0}^{N_c-1} \alpha_l g(nT - \tau_l) e^{-j\frac{2\pi kn}{N_c}} = \alpha_l e^{-j\frac{2\pi kn_l}{N_c}}$, $\delta_q[k] \triangleq \sum_{n=0}^{N_c-1} \alpha_q g(nT - \tau_q) e^{-j\frac{2\pi kn}{N_c}} = \alpha_q e^{-j\frac{2\pi kn_q}{N_c}}$, and $\delta_{q'}[k] \triangleq \sum_{n=0}^{N_c-1} \alpha_{q'} g(nT - \tau_{q'}) e^{-j\frac{2\pi kn}{N_c}} = \alpha_{q'} e^{-j\frac{2\pi kn_{q'}}{N_c}}$ with the indices n_l , n_q , and $n_{q'}$ satisfying $n_l T < \tau_l \leq (n_l + 1)T$, $n_q T < \tau_q \leq (n_q + 1)T$, and $n_{q'} T < \tau_{q'} \leq (n_{q'} + 1)T$, respectively.

Moreover, the channel model in (9) can be written in a compact form as follows

$$\mathbf{G}[k] = \mathbf{A}_{\mathbf{G}} \mathbf{\Delta}_{\mathbf{G}}[k] \bar{\mathbf{\Delta}}_{\mathbf{G}} \mathbf{B}_{\mathbf{G}}^H, \quad (12)$$

where $\mathbf{A}_{\mathbf{G}} \triangleq [\mathbf{a}_{\mathbf{G}}(\phi_0), \mathbf{a}_{\mathbf{G}}(\phi_1), \dots, \mathbf{a}_{\mathbf{G}}(\phi_{L-1})]$, $\mathbf{\Delta}_{\mathbf{G}}[k] \triangleq \text{diag} \left(e^{-j\frac{2\pi kn_0}{N_c}}, e^{-j\frac{2\pi kn_1}{N_c}}, \dots, e^{-j\frac{2\pi kn_{L-1}}{N_c}} \right)$, $\bar{\mathbf{\Delta}}_{\mathbf{G}} \triangleq \text{diag}(\alpha_0, \alpha_1, \dots, \alpha_{L-1})$, and $\mathbf{B}_{\mathbf{G}} \triangleq [\mathbf{b}_{\mathbf{G}}(\psi_0), \mathbf{b}_{\mathbf{G}}(\psi_1), \dots, \mathbf{b}_{\mathbf{G}}(\psi_{L-1})]$.

C. Power Pattern of the RIS

For the transmission of N_d streams, we can treat the power pattern as the summation of N_d patterns, each of which is generated by one column of \mathbf{W} [26]. Therefore, we obtain the power pattern reflected by the RIS, towards the angle ϕ and at the k -th subcarrier, as follows

$$y(\phi, k) = M \left\| \mathbf{a}_{\mathbf{H}}^H(\phi) \mathbf{\Theta} \mathbf{G}[k] \mathbf{W}[k] \right\|_2^2, \quad (13)$$

where $\mathbf{a}_{\mathbf{H}}(\phi)$, defined in (7), represents the steering vector towards ϕ . We omit the transmit power p and the large-scale fading factors in (13) for simplification. Note that the power pattern $y(\phi, k)$ defined in (13) differs among the subcarriers since it depends on the BS-RIS channel $\mathbf{G}[k]$ at each subcarrier.

However, the acquirement of instantaneous CSI in the RIS-assisted OFDM system requires a high overhead of training and feedback, therefore, it is viable to synthesize the pattern by using the statistical CSI between the BS and the RIS. In this way, we take the expectation of (13) and obtain the average power pattern $y(\phi)$ as follows

$$\begin{aligned} y(\phi) &= M \mathbb{E} \left\{ \|\mathbf{a}_{\mathbf{H}}^H(\phi) \Theta \mathbf{G}[k] \mathbf{W}[k]\|_2^2 \right\} \\ &= M^2 N_{\text{BS}} \mathbf{a}_{\mathbf{H}}^H(\phi) \Theta \mathbf{A}_{\mathbf{G}} \Delta_{\mathbf{G}}[k] \mathbb{E} \left\{ \bar{\Delta}_{\mathbf{G}} \mathbf{B}_{\mathbf{G}}^H \mathbf{W}[k] \mathbf{W}[k]^H \mathbf{B}_{\mathbf{G}} \bar{\Delta}_{\mathbf{G}}^H \right\} \Delta_{\mathbf{G}}^H[k] \mathbf{A}_{\mathbf{G}}^H \Theta^H \mathbf{a}_{\mathbf{H}}(\phi) \\ &= M^2 N_{\text{BS}} \mathbf{a}_{\mathbf{H}}^H(\phi) \Theta \mathbf{A}_{\mathbf{G}} \mathbf{I} \circ (\Lambda \mathbf{B}_{\mathbf{G}}^H \mathbf{W} \mathbf{W}^H \mathbf{B}_{\mathbf{G}}) \mathbf{A}_{\mathbf{G}}^H \Theta^H \mathbf{a}_{\mathbf{H}}(\phi), \end{aligned} \quad (14)$$

where $\Lambda \triangleq \mathbb{E} \left\{ \bar{\Delta}_{\mathbf{G}} \bar{\Delta}_{\mathbf{G}}^H \right\} = \text{diag} \left(\mathbb{E} \{ |\alpha_0|^2 \}, \mathbb{E} \{ |\alpha_1|^2 \}, \dots, \mathbb{E} \{ |\alpha_{L-1}|^2 \} \right)$. Note that the average power pattern derived in (14) is independent of the index of subcarrier k , therefore, the design of the precoder \mathbf{W} and the RIS phase matrix Θ is frequency-independent. Moreover, the RIS provides a quasi-static coverage for the users since the average power pattern derived in (14) relies on the statistical CSI of the channel paths, i.e., $\mathbf{A}_{\mathbf{G}}$, $\mathbf{B}_{\mathbf{G}}$, and Λ .

Remark 1: When the power pattern is synthesized by using the LoS channel between the BS and the RIS, as previously discussed in [30], we find that the power pattern in (13) and the corresponding pattern synthesis are essentially frequency-independent.

To facilitate the pattern synthesis, we oversample the continuous pattern $y(\phi)$ derived in (14) at the discrete angles of $\bar{\phi}_j = \frac{\pi}{\kappa M} j$, $j = 0, 1, \dots, \kappa M - 1$, where $\kappa > 1$. Then, we obtain the discrete power pattern \mathbf{y} as follows [26]

$$\mathbf{y} = M^2 N_{\text{BS}} \text{diag} \left(\tilde{\mathbf{A}} \Theta \mathbf{A}_{\mathbf{G}} \mathbf{I} \circ (\Lambda \mathbf{B}_{\mathbf{G}}^H \mathbf{W} \mathbf{W}^H \mathbf{B}_{\mathbf{G}}) \mathbf{A}_{\mathbf{G}}^H \Theta^H \tilde{\mathbf{A}}^H \right), \quad (15)$$

where

$$\tilde{\mathbf{A}} \triangleq [\mathbf{a}_{\mathbf{H}}(\bar{\phi}_0), \mathbf{a}_{\mathbf{H}}(\bar{\phi}_1), \dots, \mathbf{a}_{\mathbf{H}}(\bar{\phi}_{\kappa M-1})]^H. \quad (16)$$

In order to meet the requirement of the broad coverage, the reflected power at each angle in (15) needs to be synthesized into the corresponding desired value, which defines a target power pattern. To this end, we formulate the desired broad coverage by defining the target pattern in the next subsection.

D. Target Pattern

To provide a reliable broad coverage for the blocked users, the target pattern is defined as a flat-top pattern as follows

$$f(\phi) \triangleq \begin{cases} f_M, & |\phi - \phi_c| \leq \phi_{0.5}(1 - \varepsilon) \\ f_S, & |\phi - \phi_c| > \phi_{0.5}(1 + \varepsilon) \\ \mu \left(\frac{\pi[|\phi - \phi_c| - \phi_{0.5}(1 - \varepsilon)]}{2\varepsilon\phi_{0.5}} \right), & \text{otherwise,} \end{cases} \quad (17)$$

where f_M denotes the power of the flat-top beam, f_S denotes the power of the side lobe, ϕ_c denotes the angle that the center of the flat-top beam points towards, $\phi_{0.5}$ denotes half of the beamwidth of the flat-top beam, $\mu(x) \triangleq \frac{f_M + f_S}{2} + \frac{f_M - f_S}{2} \cos x$, and ε is the roll-off factor. Note that the target pattern in (17) provides a broad coverage with the constant power gain over the angle range of $[\phi_c - \phi_{0.5}, \phi_c + \phi_{0.5}]$. Then, the target pattern is discretized into a vector \mathbf{f} with the same oversampling factor κ as defined in (15).

Therefore, we can synthesize the power pattern in (15) according to the target pattern defined in (17). In the next subsection, we formulate the optimization problem of pattern synthesis.

E. Problem Formulation

To obtain the desired pattern, we synthesize the power pattern \mathbf{y} derived in (15) by jointly optimizing the precoder \mathbf{W} and the RIS phase matrix Θ . To start with, we define the cost function of the optimization problem as the distance between the power pattern \mathbf{y} and the target pattern \mathbf{f} . In [26] and [30], the cosine distance was used to depict the difference between \mathbf{y} and \mathbf{f} , where the magnitude information was not considered [34]. When using the LoS BS-RIS channel model for the design, we can decouple the BS precoder from the power pattern and handle the magnitude of the pattern independently [30]. However, when considering the multipath channel model between the BS and the RIS, the precoder \mathbf{W} has an impact on both the magnitude and the shape of the power pattern, and cannot be decoupled from the power pattern as shown in (15). The lack of magnitude information can lead to a degradation of the power gain when pursuing a well-shaped pattern. Therefore, we use a weighted Euclidean distance in the following to take the magnitude of power pattern into consideration.

As defined in (17), the target power pattern is divided into three regions: the flat-top region $\mathcal{A}_1 = \{\phi \mid |\phi - \phi_c| \leq \phi_{0.5}(1 - \varepsilon)\}$, the sidelobe region $\mathcal{A}_2 = \{\phi \mid |\phi - \phi_c| > \phi_{0.5}(1 + \varepsilon)\}$, and the roll-off transition region $\mathcal{A}_3 = \{\phi \mid \phi_{0.5}(1 - \varepsilon) < |\phi - \phi_c| \leq \phi_{0.5}(1 + \varepsilon)\}$. To obtain the desired

broad coverage, we can adopt different weights, i.e., $\bar{\gamma}_\iota \in \mathbb{R}^+$, $\iota = 1, 2, 3$, for the three regions according to their priorities. Therefore, we define the weighted Euclidean distance between \mathbf{y} and \mathbf{f} as follows

$$D(\mathbf{f}, \mathbf{y}) \triangleq \left[\sum_{j=0}^{\kappa M-1} \gamma_j (\mathbf{f}_j - \mathbf{y}_j)^2 \right]^{1/2}, \quad (18)$$

where the index j corresponds to the discrete angle $\bar{\phi}_j$, and the weight γ_j is defined as follows

$$\gamma_j \triangleq \begin{cases} \bar{\gamma}_\iota, & \bar{\phi}_j \in \mathcal{A}_\iota, \iota = 1, 3 \\ \bar{\gamma}_2, & \bar{\phi}_j \in \mathcal{A}_2 \text{ and } \mathbf{y}_j > \mathbf{f}_j \\ 0, & \bar{\phi}_j \in \mathcal{A}_2 \text{ and } \mathbf{y}_j \leq \mathbf{f}_j. \end{cases} \quad (19)$$

Note that the side lobes that are lower than the target pattern, i.e., $\mathbf{y}_j \leq \mathbf{f}_j$, are not included. By defining the weight matrix as $\mathbf{\Gamma} \triangleq \text{diag}(\sqrt{\gamma_0}, \sqrt{\gamma_1}, \dots, \sqrt{\gamma_{\kappa M-1}})$, we rewrite the weighted Euclidean distance in (18) by a compact form as follows

$$D(\mathbf{f}, \mathbf{y}) = \|\mathbf{\Gamma}(\mathbf{f} - \mathbf{y})\|_2. \quad (20)$$

Equivalently, we can formulate the optimization problem of pattern synthesis as

$$\text{P1: } \min_{\mathbf{W}, \Theta} J(\mathbf{W}, \Theta) = \|\mathbf{\Gamma}[\mathbf{f} - \mathbf{y}(\mathbf{W}, \Theta)]\|_2^2 \quad (21)$$

$$\text{s.t. } \|\mathbf{W}\|_F^2 = 1, \quad (22)$$

$$|\theta_m| = 1, \quad m = 0, 1, \dots, M-1, \quad (23)$$

where (22) and (23) are the BS transmit power constraint and the RIS phase shift constraint, respectively. Note that the normalization of the precoder, i.e., $\sum_{k=0}^{N_c-1} \|\mathbf{W}[k]\|_F^2 = N_c$ defined in (1), reduces to (22) due to the frequency-independent precoder.

In problem P1, there exists two issues on the optimization. Firstly, the variables \mathbf{W} and Θ are coupled in the cost function. Secondly, the phase shifts of the RIS are constrained by a constant modulus, which makes the optimization intractable. To address the above issues, we propose a design framework for solving problem P1 in the following section.

III. MANIFOLD OPTIMIZATION FOR PATTERN SYNTHESIS

A. Problem Reformulation

As mentioned above, problem P1 is hard to tackle and needs to be reformulated. Observing the constraint in (22), we divide \mathbf{W} by a normalization factor $\|\mathbf{W}\|_F$, and directly substitute the power constraint into the power pattern as follows

$$\bar{\mathbf{y}} = \frac{M^2 N_{\text{BS}}}{\|\mathbf{W}\|_F^2} \text{diag} \left(\tilde{\mathbf{A}} \boldsymbol{\Theta} \mathbf{A}_{\mathbf{G}} \mathbf{I} \circ (\boldsymbol{\Lambda} \mathbf{B}_{\mathbf{G}}^H \mathbf{W} \mathbf{W}^H \mathbf{B}_{\mathbf{G}}) \mathbf{A}_{\mathbf{G}}^H \boldsymbol{\Theta}^H \tilde{\mathbf{A}}^H \right). \quad (24)$$

Therefore, problem P1 is reformulated as

$$\text{P2} : \min_{\mathbf{W}, \boldsymbol{\Theta}} J(\mathbf{W}, \boldsymbol{\Theta}) = \|\boldsymbol{\Gamma} [\mathbf{f} - \bar{\mathbf{y}}(\mathbf{W}, \boldsymbol{\Theta})]\|_2^2 \quad (25)$$

$$\text{s.t. } |\theta_m| = 1, \quad m = 0, 1, \dots, M - 1. \quad (26)$$

It is observed that the variables \mathbf{W} and $\boldsymbol{\Theta}$ are coupled in (24) and (25). To handle this, we employ an alternating optimization method to obtain a locally optimal solution to problem P2, which iteratively minimizes the cost function with respect to \mathbf{W} and $\boldsymbol{\Theta}$ while keeping the other one fixed. Therefore, we have the following subproblems with respect to \mathbf{W} and $\boldsymbol{\Theta}$, respectively:

$$\text{P2.1} : \min_{\mathbf{W}} J(\mathbf{W}) = \|\boldsymbol{\Gamma} [\mathbf{f} - \bar{\mathbf{y}}(\mathbf{W})]\|_2^2 \quad (27)$$

$$\text{P2.2} : \min_{\boldsymbol{\Theta}} J(\boldsymbol{\Theta}) = \|\boldsymbol{\Gamma} [\mathbf{f} - \bar{\mathbf{y}}(\boldsymbol{\Theta})]\|_2^2 \quad (28)$$

$$\text{s.t. } |\theta_m| = 1, \quad m = 0, 1, \dots, M - 1. \quad (29)$$

Given the non-convex constant modulus constraint in (29), it is difficult to solve problem P2.2 by directly using conventional method of pattern synthesis over the Euclidean space. To overcome this problem, we regard the constant modulus constraint as a Riemannian manifold such that we can search the solution over the manifold. In the following subsections, we first optimize the precoder \mathbf{W} in problem P2.1 by using the conventional CG method. Next, we propose a manifold based CG method for problem P2.2 to optimize the phase shifts $\boldsymbol{\Theta}$ of the RIS. Then, we summarize the alternating optimization for \mathbf{W} and $\boldsymbol{\Theta}$.

B. Optimization for \mathbf{W}

For problem P2.1 with a given $\boldsymbol{\Theta}$, we can employ the conventional CG method to search the optimal \mathbf{W} [35], where the Euclidean gradient of the cost function $J(\mathbf{W})$ is derived in the following proposition.

Proposition 1: The Euclidean gradient of $J(\mathbf{W})$ has the following form:

$$\begin{aligned} \frac{\partial J}{\partial \mathbf{W}^*} &= \frac{2\mathbf{W}}{\|\mathbf{W}\|_F^2} [\text{tr}(\mathbf{\Gamma}^2 \mathbf{f} \bar{\mathbf{y}}^H) - \|\mathbf{\Gamma} \bar{\mathbf{y}}\|_2^2] \\ &\quad + \frac{2M^2 N_{\text{BS}}}{\|\mathbf{W}\|_F^2} \mathbf{B}_G \mathbf{I} \circ \left[\mathbf{A}_G^H \mathbf{\Theta}^H \tilde{\mathbf{A}}^H \mathbf{\Gamma}^2 \text{diag}(\bar{\mathbf{y}} - \mathbf{f}) \tilde{\mathbf{A}} \mathbf{\Theta} \mathbf{A}_G \right] \mathbf{\Lambda} \mathbf{B}_G^H \mathbf{W}. \end{aligned} \quad (30)$$

Proof: See Appendix A. ■

C. Manifold Optimization for $\mathbf{\Theta}$

For problem P2.2 with a given \mathbf{W} , we first derive the Euclidean gradient of the cost function $J(\mathbf{\Theta})$. Notice that $\mathbf{\Theta}$ is a structured matrix with all the non-diagonal entries equaling zero. For the ease of derivation, we regard the diagonal entries of $\mathbf{\Theta}$, i.e., $\boldsymbol{\theta} \triangleq \text{diag}(\mathbf{\Theta})$, as the optimization variable. The derivative with respect to the structured matrix is introduced in [36], accordingly, we have the following lemma.

Lemma 1: Assume that $J : \mathbb{C}^{M \times 1} \times \mathbb{C}^{M \times 1} \rightarrow \mathbb{C}$ is a scalar function of $\boldsymbol{\theta} \in \mathbb{C}^{M \times 1}$ and $\boldsymbol{\theta}^* \in \mathbb{C}^{M \times 1}$, and define $\mathbf{\Theta} \triangleq \text{diag}(\boldsymbol{\theta})$. Then, the derivatives of J with respect to $\boldsymbol{\theta}^*$ and $\mathbf{\Theta}^*$ have the following relationship:

$$\frac{\partial J}{\partial \boldsymbol{\theta}^*} = \text{diag} \left(\frac{\partial J}{\partial \mathbf{\Theta}^*} \right). \quad (31)$$

Proof: See Appendix B. ■

Based on *Lemma 1*, we derive the Euclidean gradient of the cost function of problem P2.2 in the following proposition.

Proposition 2: The Euclidean gradient of $J(\boldsymbol{\theta})$ has the following form:

$$\frac{\partial J}{\partial \boldsymbol{\theta}^*} = \frac{2M^2 N_{\text{BS}}}{\|\mathbf{W}\|_F^2} \text{diag} \left(\tilde{\mathbf{A}}^H \mathbf{\Gamma}^2 \text{diag}(\bar{\mathbf{y}} - \mathbf{f}) \tilde{\mathbf{A}} \mathbf{\Theta} \mathbf{V} \right), \quad (32)$$

where $\mathbf{V} = \mathbf{A}_G \mathbf{I} \circ (\mathbf{\Lambda} \mathbf{B}_G^H \mathbf{W} \mathbf{W}^H \mathbf{B}_G) \mathbf{A}_G^H$.

Proof: See Appendix C. ■

Next, regarding the non-convex constant modulus constraint in (29), we apply the Euclidean gradient derived in *Proposition 2* over a Riemannian manifold as follows

$$\mathcal{M} \triangleq \{ \boldsymbol{\theta} \in \mathbb{C}^{M \times 1} : |\theta_m| = 1, m = 0, 1, \dots, M-1 \}. \quad (33)$$

By treating \mathbb{C} as \mathbb{R}^2 , we define the inner product as $\langle \theta_1, \theta_2 \rangle \triangleq \Re[\theta_1 \theta_2^*]$ [37]. Then, the corresponding tangent space $\mathcal{T}_{\boldsymbol{\theta}} \mathcal{M}$ at the point $\boldsymbol{\theta}$ can be defined as [38]

$$\mathcal{T}_{\boldsymbol{\theta}} \mathcal{M} \triangleq \{ \mathbf{x} \in \mathbb{C}^{M \times 1} : \Re[\mathbf{x} \circ \boldsymbol{\theta}^*] = \mathbf{0} \}. \quad (34)$$

Given the definition of the Riemannian manifold, we can employ the CG method to search a local optimum by treating \mathcal{M} as the search space. Before introducing the algorithm, we define two kinds of projections towards the tangent space and the manifold, respectively.

Firstly, we project the Euclidean gradient onto the tangent space $\mathcal{T}_\theta\mathcal{M}$, which defines the Riemannian gradient $\nabla_\theta J$. Specifically, to project a vector \mathbf{d} onto the tangent space $\mathcal{T}_\theta\mathcal{M}$, we use the following orthogonal projection [37]:

$$P_\theta(\mathbf{d}) = \mathbf{d} - \Re[\mathbf{d} \circ \boldsymbol{\theta}^*] \circ \boldsymbol{\theta}. \quad (35)$$

We apply this projection to $\partial J(\boldsymbol{\theta})/\partial \boldsymbol{\theta}^*$, and obtain the Riemannian gradient as follows

$$\nabla_\theta J = P_\theta\left(\frac{\partial J(\boldsymbol{\theta})}{\partial \boldsymbol{\theta}^*}\right) = \frac{\partial J(\boldsymbol{\theta})}{\partial \boldsymbol{\theta}^*} - \Re\left[\frac{\partial J(\boldsymbol{\theta})}{\partial \boldsymbol{\theta}^*} \circ \boldsymbol{\theta}^*\right] \circ \boldsymbol{\theta}. \quad (36)$$

After updating the point with the Riemannian gradient, we employ another projection called retraction to project the updated point \mathbf{x} back onto the manifold, which is defined as

$$\text{Ret}(\mathbf{x}) \triangleq \left[\frac{x_0}{|x_0|}, \frac{x_1}{|x_1|}, \dots, \frac{x_{M-1}}{|x_{M-1}|} \right]. \quad (37)$$

With the above definitions of the Riemannian manifold, we propose a manifold based CG method to optimize the phase shifts of the RIS in problem P2.2, which is shown in Algorithm 1. In the light of [39, Theorem 4.3.1], Algorithm 1 is guaranteed to converge to a critical point.

Algorithm 1 Riemannian Manifold Based CG Algorithm

Input: $\boldsymbol{\theta}_0$

- 1: Set the initial search direction $\mathbf{d}_0 = -\nabla_{\boldsymbol{\theta}_0} J$ and $t = 0$
 - 2: **repeat**
 - 3: Choose the step size ω_t via the Armijo backtracking line search [39]
 - 4: Update the vector: $\boldsymbol{\theta}_{t+1} = \text{Ret}(\boldsymbol{\theta}_t + \omega_t \mathbf{d}_t)$
 - 5: Calculate the Riemannian gradient $\nabla_{\boldsymbol{\theta}_{t+1}} J$ according to (32) and (36)
 - 6: Calculate the Polak-Ribière parameter [39]:

$$\mathcal{B}_{t+1} = \frac{(\nabla_{\boldsymbol{\theta}_{t+1}} J)^H [\nabla_{\boldsymbol{\theta}_{t+1}} J - P_{\boldsymbol{\theta}_{t+1}}(\nabla_{\boldsymbol{\theta}_t} J)]}{\|\nabla_{\boldsymbol{\theta}_t} J\|_2^2}$$
 - 7: Calculate the conjugate direction:

$$\mathbf{d}_{t+1} = -\nabla_{\boldsymbol{\theta}_{t+1}} J + \mathcal{B}_{t+1} P_{\boldsymbol{\theta}_{t+1}}(\mathbf{d}_t)$$
 - 8: $t \leftarrow t + 1$
 - 9: **until** convergence.
-

In Step 3 of Algorithm 1, given the scalars $l, \gamma \in (0, 1)$ and $q > 0$, the Armijo step size is $\omega_t = ql^n$, where n is the smallest nonnegative integer that satisfies [39, Definition 4.2.2]

$$J(\boldsymbol{\theta}_t) - J(\text{Ret}(\boldsymbol{\theta}_t + ql^n \mathbf{d}_t)) \geq -\gamma ql^n \Re \left[(\nabla_{\boldsymbol{\theta}_t} J)^H \mathbf{d}_t \right]. \quad (38)$$

D. Alternating Optimization for Pattern Synthesis

We summarize the alternating optimization for problem P2 in Algorithm 2.

Algorithm 2 Alternating Optimization for the Manifold Based Pattern Synthesis of the RIS

Input: $\boldsymbol{\theta}^{(0)}, \mathbf{W}^{(0)}$

- 1: Set $t' = 0$
 - 2: **repeat**
 - 3: Fix $\boldsymbol{\theta}^{(t')}$, optimize $\mathbf{W}^{(t'+1)}$ using the CG method and *Proposition 1*
 - 4: Fix $\mathbf{W}^{(t'+1)}$, optimize $\boldsymbol{\theta}^{(t'+1)}$ using Algorithm 1
 - 5: $t' \leftarrow t' + 1$
 - 6: **until** convergence.
-

In each iteration of Algorithm 2, the value of the cost function J is non-increasing, non-negative, and locally optimal, therefore, the alternating optimization is guaranteed to converge to a locally optimal solution.

Remark 2: The design framework in Algorithm 2 considers the general multipath model for the BS-RIS channel, and jointly optimizes the precoder at the BS and the phase shifts of the RIS, which encompasses the special case discussed in [29] and [30] that adopted the LoS BS-RIS channel model to optimize the phase shifts of the RIS.

In fact, under the multipath BS-RIS channel, the reflected power pattern cannot be synthesized by directly using the sub-array based method proposed in [29]. To reveal the difference, we rewrite the power pattern in (14) as follows

$$y(\phi) = M^2 N_{\text{BS}} \sum_{l=0}^{L-1} \chi_l \mathbf{a}_{\mathbf{H}}^H(\phi) \boldsymbol{\Theta} \mathbf{a}_{\mathbf{G}}(\phi_l) \mathbf{a}_{\mathbf{G}}^H(\phi_l) \boldsymbol{\Theta}^H \mathbf{a}_{\mathbf{H}}(\phi), \quad (39)$$

where χ_l denotes the l -th diagonal entry of the matrix $\mathbf{I} \circ (\boldsymbol{\Lambda} \mathbf{B}_{\mathbf{G}}^H \mathbf{W} \mathbf{W}^H \mathbf{B}_{\mathbf{G}})$, and $\mathbf{a}_{\mathbf{G}}(\phi_l)$ is the l -th column of $\mathbf{A}_{\mathbf{G}}$ as defined in (12). From (39), we find that the power pattern reflected by the RIS is the superposition of several patterns, each of which corresponds to an impinging channel path with the AoA of ϕ_l . Accordingly, we have the following proposition.

Proposition 3: Given the phase shifts at the RIS, changing the AoA of the impinging signal leads to a shift in the AoD of the flat-top beam. Specifically, assume that the RIS reflects the signal from the AoA of ϕ_0 towards a flat-top region that covers $\mathcal{A}_1 = [\phi_{\min}, \phi_{\max}]$, $\phi_{\min}, \phi_{\max} \in [\pi/2, \pi]$. Then, changing the AoA of the impinging signal to another angle ϕ_1 ($\phi_1 \neq \phi_0$) results in a shifted flat-top region $\mathcal{A}'_1 = [\phi'_{\min}, \phi'_{\max}]$, where ϕ'_{\min} and ϕ'_{\max} are defined by

$$\begin{cases} \phi'_{\min} = \arccos(\cos \phi_{\min} + \xi), \phi'_{\max} = \arccos(\max\{-1, \cos \phi_{\max} + \xi\}), & \phi_1 < \phi_0 \\ \phi'_{\min} = \arccos(\cos \phi_{\min} + \xi), \phi'_{\max} = \arccos(\cos \phi_{\max} + \xi), & \phi_1 > \phi_0, \end{cases} \quad (40)$$

where $\xi \triangleq \cos \phi_0 - \cos \phi_1$.

Proof: See Appendix D. ■

Remark 3: It is observed in *Proposition 3* that, $\phi'_{\min} > \phi_{\min}$ and $\phi'_{\max} > \phi_{\max}$ hold for $\phi_1 < \phi_0$, while $\phi'_{\min} < \phi_{\min}$ and $\phi'_{\max} < \phi_{\max}$ hold for $\phi_1 > \phi_0$, which can be explained by the law of reflection. Moreover, the range of the shifted flat-top region is not necessarily equal to that of the original flat-top region, i.e., $\phi'_{\max} - \phi'_{\min} \neq \phi_{\max} - \phi_{\min}$, while the shape of the flat-top beam holds. Note that a similar conclusion was obtained in [27] by numerical simulations, while it is strictly proved in this paper.

From (39) and *Proposition 3*, we find that, multiple impinging channel paths with different AoAs turn the reflected pattern towards different AoDs, which leads to interference and scattering. Therefore, under the multipath BS-RIS channel, we need to synthesize the superposition of multiple reflected patterns instead of designing a single pattern based on the LoS BS-RIS channel. To this end, we propose the general design framework, i.e., Algorithm 2, in this paper.

Moreover, by using the proposed RIS-assisted broad coverage, we can provide performance enhancements in the mmWave communications of both the broadcast channel and the OFDMA channel. The detailed discussions of the applications and the corresponding performance analysis are given in the next section.

IV. APPLICATIONS AND PERFORMANCE ANALYSIS OF RIS-ASSISTED BROAD COVERAGE

A. Communications of Broadcast Channels

As for the communication of broadcast channels in an RIS-assisted massive MIMO-OFDM system, we derive the downlink rate of transmitting multiple streams as follows

$$R = \sum_{k=0}^{N_c-1} \log_2 \det \left(\mathbf{I}_{N_{\text{UE}}} + \frac{p}{\sigma_z^2} \mathbf{H}_{\text{eq}}[k] \mathbf{W}[k] \mathbf{W}^H[k] \mathbf{H}_{\text{eq}}^H[k] \right), \quad (41)$$

where $\mathbf{H}_{\text{eq}}[k] \triangleq \sqrt{\beta_1\beta_2}\mathbf{H}[k]\mathbf{\Theta}\mathbf{G}[k] + \sqrt{\beta}\mathbf{H}_d[k]$. It is difficult to derive the analytical ergodic rate from (41). Therefore, we verify the performance of the proposed broad coverage via numerical simulations in Section V. Nevertheless, we derive an analytical expression of the average received signal power at the user by ignoring the blocked BS-UE direct channel in the following theorem.

Theorem 1: Assume that the perfect power pattern is synthesized in accordance with (17), i.e., $y(\phi) = f(\phi)$, the side lobe $f_S = 0$, and the rectangular roll-off $\mathcal{A}_3 = \emptyset$, each user within the broad coverage receives an average power, across all the antennas and subcarriers, as follows

$$\mathbb{E}\{|r|^2\} = p\beta_1\beta_2f_M \sum_{\phi_q \in \mathcal{A}_1} \mathbb{E}\{|\alpha_q|^2\} + \sigma_z^2, \quad (42)$$

where \mathcal{A}_1 is the flat-top region of the power pattern defined in Section II-E, and $\sum_{\phi_q \in \mathcal{A}_1} \mathbb{E}\{|\alpha_q|^2\}$ denotes the average power of all the channel paths within the broad coverage \mathcal{A}_1 . Furthermore, without loss of generality, we assume that the channel power of NLoS paths is uniformly distributed over $[0, \pi]$, therefore, we find that each user within the broad coverage receives a constant average power as follows

$$\mathbb{E}\{|r|^2\} = p\beta_1\beta_2f_M \left[\frac{K}{K+1} + \frac{|\mathcal{A}_1|}{\pi(K+1)} \right] + \sigma_z^2, \quad (43)$$

where K is the K-factor of the RIS-UE channel, and $|\mathcal{A}_1|$ denotes the beamwidth of the power pattern reflected by the RIS.

Proof: See Appendix E. ■

Remark 4: The analytical expression in (42) indicates that, given an idealized power pattern, the received signal power of the user depends on the power gain reflected by the RIS, i.e., f_M . Then, we give the power scaling law in the following proposition.

Proposition 4: The received power of the user and the power of the flat-top beam both increase linearly with the number of RIS reflecting elements M , and decrease linearly with the beamwidth of the power pattern reflected by the RIS.

Proof: See Appendix F. ■

B. Communications of OFDMA Channels

We consider applying the quasi-static broad coverage to the scenario of OFDMA channels, where each user is assigned to a respective set of subcarriers. For multiuser multi-carrier systems, it is intractable to design a common set of RIS phase shifts for serving multiple users at each respective subcarrier. Moreover, the overhead of channel estimation and feedback is large when

the phase shifts of the RIS are optimized under the instantaneous CSI. Fortunately, the proposed broad coverage can provide quasi-static services for multiple users simultaneously, which only needs a reduced overhead of the statistical CSI. Specifically, by using the LoS BS-RIS channel, we can decouple the optimizations of the precoder at the BS and the phase shifts of the RIS [30], which facilitates an independent design for each user at the respective subcarrier. Accordingly, we consider an RIS-assisted massive MIMO-OFDMA system with multiple single-antenna users. The downlink rate of the considered system is given by

$$R' = \sum_{u=0}^{U-1} \sum_{k \in \{\mathcal{K}_u\}} \log_2 \left[1 + \frac{P}{\sigma_z^2} \left| \left(\sqrt{\beta_1 \beta_2} \mathbf{h}_u^H[k] \mathbf{\Theta} \mathbf{G}_0[k] + \sqrt{\beta} \mathbf{h}_{du}^H[k] \right) \mathbf{w}[k] \right|^2 \right], \quad (44)$$

where u denotes the index of user, U is the number of users, \mathcal{K}_u denotes the set of subcarriers allocated to the u -th user, $\mathbf{h}_u^H[k]$ is the channel between the RIS and the u -th user, $\mathbf{G}_0[k]$ is the LoS BS-RIS channel, and $\mathbf{h}_{du}^H[k]$ is the direct channel between the BS and the u -th user. Accordingly, we have

$$\mathbf{h}_u^H[k] \triangleq \sqrt{M} \sum_{q_u=0}^{Q-1} \delta_{q_u}[k] \mathbf{a}_{\mathbf{H}}^H(\phi_{q_u}), \quad (45)$$

$$\mathbf{G}_0[k] \triangleq \sqrt{N_{\text{BS}} M} \eta \mathbf{a}_{\mathbf{G}}(\phi_0) \mathbf{b}_{\mathbf{G}}^H(\psi_0), \quad (46)$$

$$\mathbf{h}_{du}^H[k] \triangleq \sqrt{N_{\text{BS}}} \sum_{q'_u=0}^{Q'-1} \delta_{q'_u}[k] \mathbf{b}_{\mathbf{G}}^H(\psi_{q'_u}), \quad (47)$$

where η is the complex phase of the LoS channel, $\delta_{q_u}[k]$ and $\delta_{q'_u}[k]$ are the frequency-domain complex gains of the q_u -th path of $\mathbf{h}_u^H[k]$ and the q'_u -th path of $\mathbf{h}_{du}^H[k]$, respectively, and ϕ_{q_u} and $\psi_{q'_u}$ are the AoDs of the q_u -th path of $\mathbf{h}_u^H[k]$ and the q'_u -th path of $\mathbf{h}_{du}^H[k]$, respectively. In detail, we define the frequency-domain complex gains, i.e., $\delta_{q_u}[k]$ and $\delta_{q'_u}[k]$, as follows

$$\delta_{q_u}[k] \triangleq \sum_{n=0}^{N_c-1} \alpha_{q_u} g(nT - \tau_{q_u}) e^{-j \frac{2\pi k n}{N_c}} = \alpha_{q_u} e^{-j \frac{2\pi k n_{q_u}}{N_c}}, \quad (48)$$

$$\delta_{q'_u}[k] \triangleq \sum_{n=0}^{N_c-1} \alpha_{q'_u} g(nT - \tau_{q'_u}) e^{-j \frac{2\pi k n}{N_c}} = \alpha_{q'_u} e^{-j \frac{2\pi k n_{q'_u}}{N_c}}, \quad (49)$$

where α_{q_u} and $\alpha_{q'_u}$ are the time-domain complex gains of the q_u -th path of the RIS-UE channel and the q'_u -th path of the BS-UE direct channel, respectively, τ_{q_u} and $\tau_{q'_u}$ are the transmission delays of the q_u -th path of the RIS-UE channel and the q'_u -th path of the BS-UE direct channel, respectively, and the indices n_{q_u} and $n_{q'_u}$ satisfy $n_{q_u} T < \tau_{q_u} \leq (n_{q_u} + 1) T$ and $n_{q'_u} T < \tau_{q'_u} \leq (n_{q'_u} + 1) T$, respectively. We assume that the time-domain channel gains, i.e., α_{q_u} and $\alpha_{q'_u}$, are all

uncorrelated and Gaussian distributed with normalized channel powers, i.e., $\sum_{q_u=0}^{Q-1} \mathbb{E}\{|\alpha_{q_u}|^2\} = 1$ and $\sum_{q'_u=0}^{Q'-1} \mathbb{E}\{|\alpha_{q'_u}|^2\} = 1$.

For any given Θ in (44), the optimal precoder that maximizes R' corresponds to the maximum ratio transmission (MRT) [40], i.e.,

$$\mathbf{w}[k] = \frac{\sqrt{\beta_1\beta_2}\mathbf{G}_0^H[k]\Theta^H\mathbf{h}_u[k] + \sqrt{\beta}\mathbf{h}_{du}[k]}{\left\|\sqrt{\beta_1\beta_2}\mathbf{G}_0^H[k]\Theta^H\mathbf{h}_u[k] + \sqrt{\beta}\mathbf{h}_{du}[k]\right\|_2}. \quad (50)$$

Then, we derive the rate in (44) as follows

$$R' = \sum_{u=0}^{U-1} \sum_{k \in \{\mathcal{K}_u\}} \log_2 \left(1 + \frac{p}{\sigma_z^2} \left\| \sqrt{\beta_1\beta_2}\mathbf{h}_u^H[k]\Theta\mathbf{G}_0[k] + \sqrt{\beta}\mathbf{h}_{du}^H[k] \right\|_2^2 \right). \quad (51)$$

From (51), we obtain the analytical rate of the considered system in the following theorem.

Theorem 2: In an RIS-assisted multiuser massive MIMO-OFDMA system, if the perfect power pattern of the RIS is synthesized in accordance with (17) and based on the LoS BS-RIS channel [30], the downlink rate can be approximated in a closed form as follows

$$\mathbb{E}\{R'\} \approx N_c \log_2 \left\{ 1 + \frac{p\beta_1\beta_2 f_M}{\sigma_z^2} \left[\frac{K}{K+1} + \frac{|\mathcal{A}_1|}{\pi(K+1)} \right] + \frac{p\beta N_{BS}}{\sigma_z^2} \right\}, \quad (52)$$

where f_M is the power of the flat-top beam defined in (17), K is the K-factor of the RIS-UE channel, and $|\mathcal{A}_1|$ denotes the beamwidth of the power pattern.

Proof: See Appendix G. ■

Remark 5: When the power gain f_M is large, the analytical rate derived in (52) increases logarithmically with f_M . Specifically, we find from *Proposition 4* that, when the number of RIS reflecting elements $M \rightarrow \infty$, the analytical rate of the considered OFDMA system increases logarithmically with M and decreases logarithmically with the beamwidth of the flat-top pattern reflected by the RIS.

Remark 6: The proposed RIS-assisted quasi-static broad coverage is well compatible with the current massive MIMO-OFDM system. Firstly, since the designs of the precoder at the BS and the phase shifts of the RIS are decoupled, the communications of the OFDMA channel and the broadcast channel can be multiplexed in the frequency domain by applying different precoders to different subcarriers while employing the same set of phase shifts at the RIS. Furthermore, we can perform the long-term update of the RIS phases with an off-line codebook such that we can improve the system performance with an unchanged frame structure, where no more time slot of training or feedback is needed for the instantaneous RIS design.

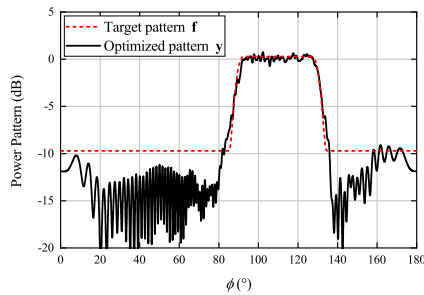


Fig. 2. Power pattern reflected by the RIS.

V. NUMERICAL RESULTS

In this section, we present the numerical simulation of the RIS-assisted broad coverage in the communications of the broadcast channel and the OFDMA channel, respectively. As shown in Fig. 1, we assume that a BS with $N_{\text{BS}} = 64$ antennas is at the origin point, an RIS is at $(190, 10)$ m, and multiple users are located around the point $(200, 0)$ m within a broad coverage over $[\phi_{\min}, \phi_{\max}]$, $\phi_{\min}, \phi_{\max} \in (0, \pi)$. For a beam covering $[\phi_{\min}, \phi_{\max}]$, the beamwidth is $2\phi_{0.5} = \phi_{\max} - \phi_{\min}$, and the steering angle is $\phi_c = (\phi_{\max} + \phi_{\min})/2$. The power pattern is oversampled by a factor of $\kappa = 10$. We define the path loss as $\text{PL} \triangleq \text{PL}_0 + 10\zeta \log_{10}(d)$, where $\text{PL}_0 = 30$ dB is the path loss at the reference distance of 1 m, ζ is the path loss exponent (PLE), and d is the distance. Then, the large-scale fading factor $\beta = 10^{-0.1\text{PL}}$. The PLEs of the BS-RIS channel, the RIS-UE channel, and the BS-UE direct channel are 2, 2.2, and 3.5, respectively. The transmit power of the BS is $p = 20$ dBm, and the noise power of the user is $\sigma_z^2 = -80$ dBm. The number of subcarriers is $N_c = 64$ and the length of the OFDM cyclic prefix (CP) is $L_{\text{CP}} = 8$. Then, the overhead of CP is considered for the rate R by calculating $\frac{N_c}{N_c + L_{\text{CP}}} R$.

A. Broadcast Channel

Firstly, we evaluate the performance of Algorithm 2. In Fig. 2, we synthesize the reflected power pattern of an RIS with $M = 100$ elements for transmitting $N_d = 4$ streams under the BS-RIS mmWave channel with $L = 5$ channel paths. In the considered multipath channel, we assume that the LoS BS-RIS channel path is as strong as the NLoS channel paths, whose profile is assumed to be uniform. It is shown in Fig. 2 that the optimized power pattern provides a broad coverage from 90° to 140° with a power fluctuation of 1.5 dB.

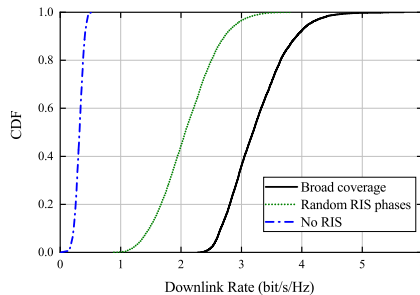


Fig. 5. CDF of the downlink rate in the communication of broadcast channel.

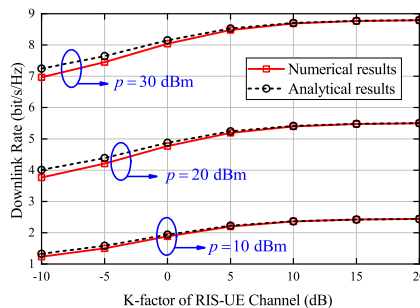


Fig. 6. Downlink rate under different K-factors of the RIS-UE channel.

the mmWave channels are randomly generated for 500 realizations. In Fig. 5, we also display the downlink rate of the random RIS phases and the downlink rate with no RIS, where the BS directly provides a broad coverage for the users. It is observed that the broad coverage designed by the proposed algorithm obtains the highest downlink rate, which verifies its effectiveness.

B. OFDMA Channel

In this subsection, we present the performance of the RIS-assisted broad coverage in OFDMA channels. In the considered OFDMA system, we design a broad coverage from 90° to 120° by assuming an RIS with $M = 200$ reflecting elements.

Firstly, we present the ergodic downlink rate under different channels and different transmit powers. In Fig. 6, we compare the analytical expression derived in (52) with the numerical results based on the instantaneous rate in (51). We assume a dominant LoS channel between the BS and the RIS. For the RIS-UE channel, we assume the uniform profile with three NLoS mmWave channel paths, and change the K-factor from -10 dB to 20 dB. For the BS-UE direct channel, we assume that the LoS channel path is blocked, and the NLoS mmWave channel paths

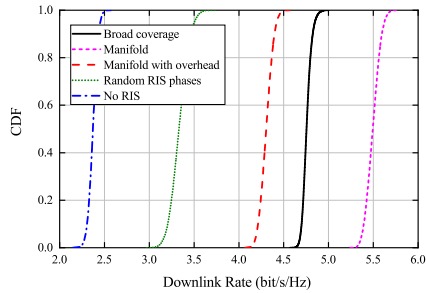


Fig. 7. CDF of the downlink rate for the OFDMA channel.

follow a uniform profile. The AoAs and the AoDs of mmWave channel paths are assumed to be uniformly distributed. We average the downlink rate of the considered OFDMA system over 1000 randomly generated channels, where the transmit power of the BS changes from 10 dBm to 30 dBm. It is found in Fig. 6 that the analytical downlink rate derived in (52) matches the numerical results well. At the small K-factors, the approximation errors between the analytical results and the numerical results are slightly larger due to the larger differences among the channel powers at the BS antennas, which leads to a larger approximation error in (71) [41].

In Fig. 7, we display the CDF of the downlink rate of the considered OFDMA system. For the BS-RIS channel and the RIS-UE channel, we assume uniform profiles with four mmWave paths for the NLoS channels and set the K-factors to 10 dB. The AoAs and AoDs of the mmWave channel paths are assumed to be uniformly distributed. We compare the performance of the proposed algorithm with the manifold method [31], which maximizes the downlink rate by using the instantaneous CSI. From Fig. 7, we find that, compared with the scenarios of the random RIS phases and no RIS, both the proposed broad coverage and the manifold method improve the downlink system rate. It is apparent that the manifold method with the perfect instantaneous CSI outperforms the broad coverage with the statistical CSI. However, the manifold method loses its advantage if we consider the estimation error of the instantaneous CSI and the overhead of channel estimation. In Fig. 7, we assume an estimation error with the normalized mean squared error (NMSE) of 0.2 for the manifold method, and assume that 20% of the coherence time is used for the channel estimation in a relative short coherence block length. For instance, in a coherence block length of ten OFDM symbols, two symbols are allocated for the channel estimation, whose overhead is calculated by adopting the grouping method introduced in [15] with a grouping ratio of 1/200. Considering the estimation error and the overhead of channel

estimation, it is found in Fig. 7 that the downlink rate of the manifold method is lower than that of the proposed quasi-static broad coverage.

VI. CONCLUSION

In this paper, we design the quasi-static broad coverage at the RIS to provide reliable mmWave communications with reduced overhead instead of optimizing the phase shifts of the RIS based on the instantaneous CSI. We propose a general design framework to synthesize the flat-top pattern with small power fluctuations. For the communication of broadcast channels, we generalize the broad coverage of the single transmit stream to the scenario of multiple streams. For the communication of OFDMA channels, we find that, by taking into account the overhead of channel estimation, the proposed quasi-static broad coverage can achieve a higher rate than the optimal RIS design that adopts the instantaneous CSI. Moreover, we derive the analytical downlink rate of the considered OFDMA system, which scales logarithmically with the power gain reflected by the RIS.

APPENDIX A

PROOF OF Proposition 1

By defining $c \triangleq M^2 N_{\text{BS}} / \|\mathbf{W}\|_F^2$, $\mathbf{V} \triangleq \mathbf{A}_G \mathbf{I} \circ (\Lambda \mathbf{B}_G^H \mathbf{W} \mathbf{W}^H \mathbf{B}_G) \mathbf{A}_G^H$, $\mathbf{Y} \triangleq \Gamma \tilde{\mathbf{A}} \Theta \mathbf{V} \Theta^H \tilde{\mathbf{A}}^H$, and $\mathbf{F} \triangleq \text{diag}(\Gamma \mathbf{f})$, we derive the cost function of problem P2 as follows

$$J = \|\Gamma(\mathbf{f} - \bar{\mathbf{y}})\|_2^2 = \|\Gamma \mathbf{f}\|_2^2 + c^2 \text{tr}(\mathbf{Y} \circ \mathbf{Y}) - 2 \text{ctr}(\mathbf{F} \mathbf{Y}^H). \quad (53)$$

Firstly, we obtain the derivatives of $1/\|\mathbf{W}\|_F^4$ and $1/\|\mathbf{W}\|_F^2$ as follows

$$\frac{d\left(\frac{1}{\|\mathbf{W}\|_F^4}\right)}{d\mathbf{W}^*} = \frac{-2\mathbf{W}}{[\text{tr}(\mathbf{W} \mathbf{W}^H)]^3}, \quad \frac{d\left(\frac{1}{\|\mathbf{W}\|_F^2}\right)}{d\mathbf{W}^*} = \frac{-\mathbf{W}}{[\text{tr}(\mathbf{W} \mathbf{W}^H)]^2}. \quad (54)$$

Then, we have the derivative of $\text{tr}(\mathbf{Y} \circ \mathbf{Y})$ as follows

$$\begin{aligned} \frac{\partial(\text{tr}(\mathbf{Y} \circ \mathbf{Y}))}{\partial \mathbf{W}^*} &\stackrel{(a)}{=} \frac{2 \text{tr}\left(\left(\mathbf{I} \circ \mathbf{Y}^T\right) \Gamma \tilde{\mathbf{A}} \Theta \mathbf{A}_G \mathbf{I} \circ \left(\Lambda \mathbf{B}_G^H \mathbf{W} d(\mathbf{W}^H) \mathbf{B}_G\right) \mathbf{A}_G^H \Theta^H \tilde{\mathbf{A}}^H\right)}{d\mathbf{W}^*} \\ &\stackrel{(b)}{=} \frac{2 \text{tr}\left(\mathbf{I} \circ \left[\mathbf{A}_G^H \Theta^H \tilde{\mathbf{A}}^H \left(\mathbf{I} \circ \mathbf{Y}^T\right) \Gamma \tilde{\mathbf{A}} \Theta \mathbf{A}_G\right] \Lambda \mathbf{B}_G^H \mathbf{W} d(\mathbf{W}^H) \mathbf{B}_G\right)}{d\mathbf{W}^*} \\ &= 2 \mathbf{B}_G \mathbf{I} \circ \left[\mathbf{A}_G^H \Theta^H \tilde{\mathbf{A}}^H \left(\mathbf{I} \circ \mathbf{Y}^T\right) \Gamma \tilde{\mathbf{A}} \Theta \mathbf{A}_G\right] \Lambda \mathbf{B}_G^H \mathbf{W}, \end{aligned} \quad (55)$$

where the equations (a) and (b) hold from the following identity [42]:

$$\text{tr}(\mathbf{A}(\mathbf{B} \circ \mathbf{C})) = \text{tr}((\mathbf{A} \circ \mathbf{B}^T) \mathbf{C}). \quad (56)$$

Moreover, the derivative of $\text{tr}(\mathbf{F}\mathbf{Y}^H)$ is derived as follows

$$\begin{aligned} \frac{\partial(\text{tr}(\mathbf{F}\mathbf{Y}^H))}{\partial\mathbf{W}^*} &= \frac{\text{tr}\left(\mathbf{F}\tilde{\mathbf{A}}\Theta\mathbf{A}_G\mathbf{I} \circ [\Lambda\mathbf{B}_G^H\mathbf{W}d(\mathbf{W}^H)\mathbf{B}_G]\mathbf{A}_G^H\Theta^H\tilde{\mathbf{A}}^H\Gamma\right)}{d\mathbf{W}^*} \\ &= \mathbf{B}_G\mathbf{I} \circ \left(\mathbf{A}_G^H\Theta^H\tilde{\mathbf{A}}^H\Gamma\mathbf{F}\tilde{\mathbf{A}}\Theta\mathbf{A}_G\right)\Lambda\mathbf{B}_G^H\mathbf{W}. \end{aligned} \quad (57)$$

Then, from (53), we derive the gradient of the cost function J as follows

$$\begin{aligned} \frac{\partial J}{\partial\mathbf{W}^*} &= M^4 N_{\text{BS}}^2 \frac{d\left(\frac{1}{\|\mathbf{W}\|_F^4}\right)}{d\mathbf{W}^*} \text{tr}(\mathbf{Y} \circ \mathbf{Y}) + \left(\frac{M^2 N_{\text{BS}}}{\|\mathbf{W}\|_F^2}\right)^2 \frac{d(\text{tr}(\mathbf{Y} \circ \mathbf{Y}))}{d\mathbf{W}^*} \\ &\quad - 2M^2 N_{\text{BS}} \frac{d\left(\frac{1}{\|\mathbf{W}\|_F^2}\right)}{d\mathbf{W}^*} \text{tr}(\mathbf{F}\mathbf{Y}^H) - \frac{2M^2 N_{\text{BS}}}{\|\mathbf{W}\|_F^2} \frac{d(\text{tr}(\mathbf{F}\mathbf{Y}^H))}{d\mathbf{W}^*}. \end{aligned} \quad (58)$$

Substituting (54)-(57) into (58), it yields (30).

APPENDIX B

PROOF OF Lemma 1

Since there exist dependencies among the entries of the diagonal matrix Θ^* [36], we define a parameterization function $\mathbf{F}(\boldsymbol{\theta}^*) \triangleq \Theta^*$, and regard the cost function J as the following composed function:

$$J(\boldsymbol{\theta}^*) = J(\tilde{\Theta}^*)|_{\tilde{\Theta}^* = \Theta^* = \mathbf{F}(\boldsymbol{\theta}^*)} = J(\mathbf{F}(\boldsymbol{\theta}^*)), \quad (59)$$

where $\tilde{\Theta}^* \in \mathbb{C}^{M \times M}$ is a matrix with independent entries [36].

To unify the format of derivative, we follow the definition in [36, Definition 3.2], and give the derivative of \mathbf{F} with respect to the complex matrix \mathbf{Z}^* as follows

$$\mathcal{D}_{\mathbf{Z}^*}\mathbf{F}(\mathbf{Z}, \mathbf{Z}^*) = \frac{\partial \text{vec}(\mathbf{F}(\mathbf{Z}, \mathbf{Z}^*))}{\partial \text{vec}^T(\mathbf{Z}^*)}. \quad (60)$$

Then, we use the chain rule of complex-valued derivatives [36], and obtain

$$\mathcal{D}_{\boldsymbol{\theta}^*}J(\boldsymbol{\theta}^*) = \left(\mathcal{D}_{\tilde{\Theta}^*}J(\tilde{\Theta}^*)|_{\tilde{\Theta}^* = \Theta^* = \mathbf{F}(\boldsymbol{\theta}^*)}\right)\mathcal{D}_{\boldsymbol{\theta}^*}\mathbf{F}. \quad (61)$$

As for $\mathcal{D}_{\boldsymbol{\theta}^*}\mathbf{F}$, we find that

$$d\text{vec}(\Theta^*) = d\text{vec}(\mathbf{F}(\boldsymbol{\theta}^*)) = \mathbf{L}_D d\boldsymbol{\theta}^*, \quad (62)$$

where \mathbf{L}_D is an $M^2 \times M$ matrix that places the diagonal entries of $\mathbf{A} \in \mathbb{C}^{M \times M}$ onto $\text{vec}(\mathbf{A})$ [36], i.e., $\text{vec}(\mathbf{I} \circ \mathbf{A}) = \mathbf{L}_D \text{diag}(\mathbf{A})$. Therefore, we have $\mathcal{D}_{\boldsymbol{\theta}^*}\mathbf{F} = \mathbf{L}_D$.

We rewrite both sides of (61) by using the formal derivative given in (60), and obtain

$$\left[\text{vec}\left(\frac{\partial J}{\partial \boldsymbol{\theta}^*}\right)\right]^T = \left[\text{vec}\left(\frac{\partial J}{\partial \tilde{\Theta}^*}\right)\Big|_{\tilde{\Theta}^* = \Theta^*}\right]^T \mathbf{L}_D \stackrel{(a)}{=} \left[\text{diag}\left(\frac{\partial J}{\partial \tilde{\Theta}^*}\Big|_{\tilde{\Theta}^* = \Theta^*}\right)\right]^T, \quad (63)$$

where (a) holds since $\mathbf{L}_D^T \text{vec}(\mathbf{A}) = \text{diag}(\mathbf{A})$ [36]. From (63), we obtain (31).

APPENDIX C

PROOF OF *Proposition 2*

From *Lemma 1*, we obtain the derivatives of the terms in (53) with respect to $\boldsymbol{\theta}^*$ as follows

$$\begin{aligned} \frac{\partial (\text{tr}(\mathbf{Y} \circ \mathbf{Y}))}{\partial \boldsymbol{\theta}^*} &\stackrel{(a)}{=} \text{diag} \left(\frac{2 \text{tr} \left((\mathbf{I} \circ \mathbf{Y}^T) \boldsymbol{\Gamma} \tilde{\mathbf{A}} \boldsymbol{\Theta} \mathbf{V} d(\boldsymbol{\Theta}^H) \tilde{\mathbf{A}}^H \right)}{d\boldsymbol{\Theta}^*} \right) \\ &= \text{diag} \left(2 \tilde{\mathbf{A}}^H (\mathbf{I} \circ \mathbf{Y}^T) \boldsymbol{\Gamma} \tilde{\mathbf{A}} \boldsymbol{\Theta} \mathbf{V} \right), \end{aligned} \quad (64)$$

$$\frac{\partial (\text{tr}(\mathbf{F} \mathbf{Y}^H))}{\partial \boldsymbol{\theta}^*} = \text{diag} \left(\frac{\text{tr} \left(\mathbf{F} \tilde{\mathbf{A}} \boldsymbol{\Theta} \mathbf{V} d(\boldsymbol{\Theta}^H) \tilde{\mathbf{A}}^H \boldsymbol{\Gamma} \right)}{d\boldsymbol{\Theta}^*} \right) = \text{diag} \left(\tilde{\mathbf{A}}^H \boldsymbol{\Gamma} \mathbf{F} \tilde{\mathbf{A}} \boldsymbol{\Theta} \mathbf{V} \right), \quad (65)$$

where the identity (56) is used in (a).

From (64)-(65) and (53), we derive the gradient of J as follows

$$\frac{\partial J}{\partial \boldsymbol{\theta}^*} = \text{diag} \left(\tilde{\mathbf{A}}^H [2c^2 (\mathbf{I} \circ \mathbf{Y}^T) \boldsymbol{\Gamma} - 2c \boldsymbol{\Gamma} \mathbf{F}] \tilde{\mathbf{A}} \boldsymbol{\Theta} \mathbf{V} \right), \quad (66)$$

from which we obtain (32).

APPENDIX D

PROOF OF *Proposition 3*

By synthesizing the power pattern based on an LoS BS-RIS channel path with the AoA of ϕ_0 , we obtain the reflected power pattern $y_L(\phi)$ towards the AoD of ϕ as follows [30]

$$y_L(\phi) = N_{\text{BS}} M^2 \left| \mathbf{a}_{\mathbf{H}}^H(\phi) \boldsymbol{\Theta} \mathbf{a}_{\mathbf{G}}(\phi_0) \right|^2. \quad (67)$$

Then, we consider another incident BS-RIS channel path with the AoA of ϕ_1 ($\phi_1 \neq \phi_0$), and rewrite the term $\mathbf{a}_{\mathbf{H}}^H(\phi) \boldsymbol{\Theta} \mathbf{a}_{\mathbf{G}}(\phi_0)$ in (67) as follows

$$\begin{aligned} \mathbf{a}_{\mathbf{H}}^H(\phi) \boldsymbol{\Theta} \mathbf{a}_{\mathbf{G}}(\phi_0) &= \frac{1}{M} \sum_{m=0}^{M-1} e^{-j \frac{2\pi}{\lambda} m \rho \cos \phi} \theta_m e^{-j \frac{2\pi}{\lambda} m \rho \cos \phi_0} \\ &= \frac{1}{M} \sum_{m=0}^{M-1} e^{-j \frac{2\pi}{\lambda} m \rho (\cos \phi + \xi)} \theta_m e^{-j \frac{2\pi}{\lambda} m \rho \cos \phi_1}, \end{aligned} \quad (68)$$

where $\xi \triangleq \cos \phi_0 - \cos \phi_1$. Observing (68), we have $y_L(\phi) = y_L(\phi')$ if there exists ϕ' satisfying $\cos \phi' = \cos \phi + \xi$, which means that the flat-top beam at the angle of ϕ is shifted to the angle of ϕ' . Since cosine function is monotonous within $[0, \pi]$, the region of the shifted flat-top beam can be determined by solving the equations $\cos \phi'_{\min} = \cos \phi_{\min} + \xi$ and $\cos \phi'_{\max} = \cos \phi_{\max} + \xi$ at the bounds of the flat-top beam $\mathcal{A}_1 = [\phi_{\min}, \phi_{\max}]$. If $\cos \phi + \xi > 1$ or $\cos \phi + \xi < -1$, the shifted

flat-top beam is partly cut off by the range of $[0, \pi]$. In detail, when $\phi_1 < \phi_0$, if $\cos \phi_{\max} + \xi < -1$, we obtain the cut-off bound $\phi'_{\max} = \pi$. Therefore, $\phi'_{\max} = \arccos(\cos \phi_{\max} + \xi)$ or $\phi'_{\max} = \pi$. Moreover, when $\phi_1 > \phi_0$, since we assume that $\phi_{\min}, \phi_{\max} \in [\pi/2, \pi]$, $\cos \phi_{\min} + \xi < 1$ holds. From the above discussions, we obtain the region of the shifted flat-top beam in (40).

APPENDIX E

PROOF OF *Theorem 1*

For a given user within the broad coverage, located at the angle of ϕ_q , the average received power at the i -th antenna is

$$\begin{aligned} \mathbb{E}\{|\mathbf{r}_i[k]|^2\} &= p\beta_1\beta_2M\mathbb{E}\left\{\left\|\sum_{q=0}^{Q-1}\delta_q[k]e^{-j\frac{2\pi}{\lambda}(i-1)\rho\sin\psi'_q}\mathbf{a}_{\mathbf{H}}^H(\phi_q)\Theta\mathbf{G}[k]\mathbf{W}[k]\mathbf{s}[k]\right\|_2^2\right\} + \sigma_z^2 \\ &\stackrel{(a)}{=} p\beta_1\beta_2M\left(\sum_{\phi_q\in\mathcal{A}_1} + \sum_{\phi_q\notin\mathcal{A}_1}\right)\mathbb{E}\{|\delta_q[k]|^2\}\mathbb{E}\left\{\left\|\mathbf{a}_{\mathbf{H}}^H(\phi_q)\Theta\mathbf{G}[k]\mathbf{W}[k]\mathbf{s}[k]\right\|_2^2\right\} + \sigma_z^2 \\ &\stackrel{(b)}{=} p\beta_1\beta_2f_M\sum_{\phi_q\in\mathcal{A}_1}\mathbb{E}\{|\alpha_q|^2\} + \sigma_z^2. \end{aligned} \quad (69)$$

In (a), the independence of the channel path is applied. In (b), we substitute the power pattern sampled at the angle ϕ_q , i.e., $y(\phi_q)$ defined in (14). Then, by using the assumption of the perfect pattern synthesis, i.e., $y(\phi) = f(\phi)$, the side lobe $f_S = 0$, and the rectangular roll-off $\mathcal{A}_3 = \emptyset$, we observe that $y(\phi_q) = f(\phi_q) = 0$ holds for $\phi_q \notin \mathcal{A}_1$, while $y(\phi_q) = f(\phi_q) = f_M$ holds for $\phi_q \in \mathcal{A}_1$. Without loss of generality, we assume that the K-factor of the RIS-UE channel is K and the channel power of the NLoS paths is uniformly distributed over $[0, \pi]$. In this way, only the LoS RIS-UE channel path and $|\mathcal{A}_1|/\pi$ of the NLoS RIS-UE channel paths are within the broad coverage, i.e., $\phi_q \in \mathcal{A}_1$. Therefore, we replace the term $\sum_{\phi_q\in\mathcal{A}_1}\mathbb{E}\{|\alpha_q|^2\}$ in (69) by $K/(K+1) + |\mathcal{A}_1|/[\pi(K+1)]$, which results in a constant average power as given in (43).

APPENDIX F

PROOF OF *Proposition 4*

The power of flat-top beam, i.e., f_M , is the product of the incident power at the RIS and the array gain of the RIS. Firstly, the overall power impinging the RIS increases linearly with the number of RIS reflecting elements, i.e., M . On the other hand, as discussed in [43], the gain \tilde{f} of an array is defined as

$$\tilde{f} \triangleq \mu D = \frac{41253^\square}{\theta_{\text{HP}}^\circ \phi_{\text{HP}}^\circ}, \quad (70)$$

where μ ($0 \leq \mu \leq 1$) is the efficiency factor, D is the directivity of the array, $41253 \approx 4\pi(180/\pi)^2$ is the number of square degrees ($^\square$) in sphere, and θ_{HP}° and ϕ_{HP}° are the half-power beamwidths in two principal planes, i.e., the elevation and the azimuth, respectively. For a linear array, the angle of elevation θ_{HP}° is a constant. Therefore, the array gain of the RIS decreases linearly with the beamwidth of the power pattern defined in (17).

APPENDIX G

PROOF OF *Theorem 2*

From (51), we approximate the downlink rate $\mathbb{E}\{R'\}$ by using [41, Lemma 1] as follows

$$\mathbb{E}\{R'\} \approx \sum_{u=0}^{U-1} \sum_{k \in \{\mathcal{K}_u\}} \log_2 \left(1 + \frac{p}{\sigma_z^2} \mathbb{E} \left\{ \left\| \sqrt{\beta_1 \beta_2} \mathbf{h}_u^H[k] \Theta \mathbf{G}_0[k] + \sqrt{\beta} \mathbf{h}_{\text{du}}^H[k] \right\|_2^2 \right\} \right), \quad (71)$$

where the approximation becomes tighter as the number of BS antennas increases [41]. Then, we derive the expectation of the terms in (71) separately. Firstly, from (47), we obtain

$$\mathbb{E} \left\{ \left\| \mathbf{h}_{\text{du}}^H[k] \right\|_2^2 \right\} = N_{\text{BS}} \sum_{q_u=0}^{Q'-1} \mathbb{E} \{ |\alpha_{q_u}|^2 \} = N_{\text{BS}}. \quad (72)$$

Then, from (45) and (46), we obtain

$$\begin{aligned} \mathbb{E} \left\{ \left\| \mathbf{h}_u^H[k] \Theta \mathbf{G}_0[k] \right\|_2^2 \right\} &= N_{\text{BS}} M^2 \mathbb{E} \left\{ \left\| \sum_{q_u=0}^{Q-1} \delta_{q_u}[k] \mathbf{a}_{\text{H}}^H(\phi_{q_u}) \Theta \eta \mathbf{a}_{\text{G}}(\phi_0) \mathbf{b}_{\text{G}}^H(\psi_0) \right\|_2^2 \right\} \\ &\stackrel{(a)}{=} \sum_{q_u=0}^{Q-1} \mathbb{E} \{ |\alpha_{q_u}|^2 \} y_{\text{L}}(\phi_{q_u}) \\ &\stackrel{(b)}{=} f_{\text{M}} \sum_{\phi_{q_u} \in \mathcal{A}_1} \mathbb{E} \{ |\alpha_{q_u}|^2 \} \\ &= f_{\text{M}} \left[\frac{K}{K+1} + \frac{|\mathcal{A}_1|}{\pi(K+1)} \right], \end{aligned} \quad (73)$$

where (67) is substituted in (a), \mathcal{A}_1 is the flat-top region of the power pattern. In (b), the assumption of the perfect pattern synthesis is used as in *Theorem 1*, i.e., $y(\phi) = f(\phi)$, the side lobe $f_{\text{S}} = 0$, and the rectangular roll-off $\mathcal{A}_3 = \emptyset$. Furthermore, by assuming that the power of NLoS RIS-UE channel paths is uniformly distributed over $[0, \pi]$, we can replace the term $\sum_{\phi_{q_u} \in \mathcal{A}_1} \mathbb{E} \{ |\alpha_{q_u}|^2 \}$ in (73) by $K/(K+1) + |\mathcal{A}_1|/[\pi(K+1)]$ as previously derived in (69).

By substituting (72) and (73) into (71), we find that the analytical rate has the same expression at each subcarrier, therefore, we replace $\sum_{u=0}^{U-1} \sum_{k \in \{\mathcal{K}_u\}}$ in (71) by N_{c} and obtain (52).

REFERENCES

- [1] Q. Wu and R. Zhang, "Towards smart and reconfigurable environment: Intelligent reflecting surface aided wireless network," *IEEE Commun. Mag.*, vol. 58, no. 1, pp. 106–112, Nov. 2019.
- [2] M. Di Renzo *et al.*, "Smart radio environments empowered by reconfigurable intelligent surfaces: How it works, state of research, and the road ahead," *IEEE J. Sel. Areas Commun.*, vol. 38, no. 11, pp. 2450–2525, Nov. 2020.
- [3] H. Shen, W. Xu, S. Gong, Z. He, and C. Zhao, "Secrecy rate maximization for intelligent reflecting surface assisted multi-antenna communications," *IEEE Commun. Lett.*, vol. 23, no. 9, pp. 1488–1492, Jun. 2019.
- [4] S. Zhou, W. Xu, K. Wang, M. Di Renzo, and M. S. Alouini, "Spectral and energy efficiency of IRS-assisted MISO communication with hardware impairments," *IEEE Wireless Commun. Lett.*, vol. 9, no. 9, pp. 1366–1369, Sep. 2020.
- [5] H. Shen, T. Ding, W. Xu, and C. Zhao, "Beamforming design with fast convergence for IRS-aided full-duplex communication," *IEEE Commun. Lett.*, vol. 24, no. 12, pp. 2849–2853, Dec. 2020.
- [6] Z. Yang, W. Xu, C. Huang, J. Shi, and M. Shikh-Bahaei, "Beamforming design for multiuser transmission through reconfigurable intelligent surface," *IEEE Trans. on Commun.*, vol. 69, no. 1, pp. 589–601, Jan. 2021.
- [7] H. Shen, W. Xu, S. Gong, C. Zhao, and D. W. K. Ng, "Beamforming optimization for IRS-aided communications with transceiver hardware impairments," *IEEE Trans. on Commun.*, vol. 69, no. 2, pp. 1214–1227, Feb. 2021.
- [8] M. Di Renzo *et al.*, "Smart radio environments empowered by reconfigurable AI meta-surfaces: An idea whose time has come," *EURASIP J. Wireless Commun. Netw.*, vol. 2019, no. 1, pp. 1–20, May 2019.
- [9] M. Di Renzo *et al.*, "Reconfigurable intelligent surfaces vs. relaying: Differences, similarities, and performance comparison," *IEEE Open J. Commun. Soc.*, vol. 1, pp. 798–807, Jun. 2020.
- [10] Y. Zhao, W. Xu, H. Sun, D. W. K. Ng, and X. You, "Cooperative reflection design with timing offsets in distributed multi-RIS communications," *IEEE Wireless Commun. Lett.*, pp. 1–1, 2021, early access.
- [11] N. S. Perović, M. D. Renzo, and M. F. Flanagan, "Channel capacity optimization using reconfigurable intelligent surfaces in indoor mmWave environments," in *Proc. IEEE Int. Conf. Commun. (ICC)*, Dublin, Ireland, Jun. 2020, pp. 1–7.
- [12] P. Wang, J. Fang, L. Dai, and H. Li, "Joint transceiver and large intelligent surface design for massive MIMO mmWave systems," *IEEE Trans. Wireless Commun.*, vol. 20, no. 2, pp. 1052–1064, Feb. 2021.
- [13] W. Zhang, J. Xu, W. Xu, D. W. K. Ng, and H. Sun, "Cascaded channel estimation for IRS-assisted mmWave multi-antenna with quantized beamforming," *IEEE Commun. Lett.*, vol. 25, no. 2, pp. 593–597, Feb. 2021.
- [14] C. Pradhan, A. Li, L. Song, B. Vucetic, and Y. Li, "Hybrid precoding design for reconfigurable intelligent surface aided mmWave communication systems," *IEEE Wireless Commun. Lett.*, vol. 9, no. 7, pp. 1041–1045, Jul. 2020.
- [15] Y. Yang, B. Zheng, S. Zhang, and R. Zhang, "Intelligent reflecting surface meets OFDM: Protocol design and rate maximization," *IEEE Trans. Commun.*, vol. 68, no. 7, pp. 4522–4535, Jul. 2020.
- [16] S. Zhang and R. Zhang, "Capacity characterization for intelligent reflecting surface aided MIMO communication," *IEEE J. Sel. Areas Commun.*, vol. 38, no. 8, pp. 1823–1838, Aug. 2020.
- [17] B. Zheng and R. Zhang, "Intelligent reflecting surface-enhanced OFDM: Channel estimation and reflection optimization," *IEEE Wireless Commun. Lett.*, vol. 9, no. 4, pp. 518–522, Apr. 2019.
- [18] H. Li *et al.*, "Intelligent reflecting surface enhanced wideband MIMO-OFDM communications: From practical model to reflection optimization," *IEEE Trans. Commun.*, vol. 69, no. 7, pp. 4807–4820, Jul. 2021.
- [19] W. Tang *et al.*, "Wireless communications with reconfigurable intelligent surface: Path loss modeling and experimental measurement," *IEEE Trans. Wireless Commun.*, vol. 20, no. 1, pp. 421–439, Jan. 2021.
- [20] B. Zheng, C. You, and R. Zhang, "Intelligent reflecting surface assisted multi-user OFDMA: Channel estimation and training design," *IEEE Trans. Wireless Commun.*, vol. 19, no. 12, pp. 8315–8329, Dec. 2020.

- [21] L. You, J. Xiong, D. W. K. Ng, C. Yuen, W. Wang, and X. Gao, "Energy efficiency and spectral efficiency tradeoff in RIS-aided multiuser MIMO uplink transmission," *IEEE Trans. Signal Process.*, vol. 69, pp. 1407–1421, Dec. 2020.
- [22] Q. U. A. Nadeem, A. Chaaban, and M. Debbah, "Opportunistic beamforming using an intelligent reflecting surface without instantaneous CSI," *IEEE Wireless Commun. Lett.*, vol. 10, no. 1, pp. 146–150, Jan. 2020.
- [23] Y. Gao, J. Xu, W. Xu, D. W. K. Ng, and M. S. Alouini, "Distributed IRS with statistical passive beamforming for MISO communications," *IEEE Wireless Commun. Lett.*, vol. 10, no. 2, pp. 221–225, Feb. 2021.
- [24] X. Meng, X. Gao, and X.-G. Xia, "Omnidirectional precoding based transmission in massive MIMO systems," *IEEE Trans. Commun.*, vol. 64, no. 1, pp. 174–186, Jan. 2016.
- [25] X. Meng, X.-G. Xia, and X. Gao, "Omnidirectional space-time block coding for common information broadcasting in massive MIMO systems," *IEEE Trans. Wireless Commun.*, vol. 17, no. 3, pp. 1407–1417, Mar. 2018.
- [26] W. Guo, A. Lu, X. Meng, X. Gao, and N. Ma, "Broad coverage precoding design for massive MIMO with manifold optimization," *IEEE Trans. Commun.*, vol. 67, no. 4, pp. 2792–2806, Dec. 2019.
- [27] V. Jamali, M. Najafi, R. Schober, and H. V. Poor, "Power efficiency, overhead, and complexity tradeoff of IRS codebook design—quadratic phase-shift profile," *IEEE Commun. Lett.*, vol. 25, no. 6, pp. 2048–2052, Jun. 2021.
- [28] Z. Xiao, T. He, P. Xia, and X.-G. Xia, "Hierarchical codebook design for beamforming training in millimeter-wave communication," *IEEE Tran. Wireless Commun.*, vol. 15, no. 5, pp. 3380–3392, May 2016.
- [29] H. Lu, Y. Zeng, S. Jin, and R. Zhang, "Aerial intelligent reflecting surface: Joint placement and passive beamforming design with 3D beam flattening," *IEEE Trans. Wireless Commun.*, vol. 20, no. 7, pp. 4128–4143, Jul. 2021.
- [30] M. He, W. Xu, and C. Zhao, "RIS-assisted broad coverage for mmWave massive MIMO system," in *2020 IEEE Int. Conf. Commun. Workshops (ICC Workshops)*, Jun. 2021, pp. 1–6.
- [31] X. Yu, D. Xu, and R. Schober, "MISO wireless communication systems via intelligent reflecting surfaces: (invited paper)," in *Proc. IEEE/CIC Int. Conf. Commun. China (ICCC)*, Changchun, China, Aug. 2019, pp. 735–740.
- [32] Z. Gao, C. Hu, L. Dai, and Z. Wang, "Channel estimation for millimeter-wave massive MIMO with hybrid precoding over frequency-selective fading channels," *IEEE Commun. Lett.*, vol. 20, no. 6, pp. 1259–1262, Jun. 2016.
- [33] K. Venugopal, A. Alkhateeb, N. González Prelicic, and R. W. Heath Jr., "Channel estimation for hybrid architecture-based wideband millimeter wave systems," *IEEE J. Sel. Areas Commun.*, vol. 35, no. 9, pp. 1996–2009, Sep. 2017.
- [34] P.-N. Tan, M. Steinbach, and V. Kumar, *Introduction to data mining*. Reading, MA, USA: Addison-Wesley, 2015.
- [35] D. P. Bertsekas, *Nonlinear Programming*, 2nd ed. Belmont, MA: Athena Scientific, 1999.
- [36] A. Hjørungnes, *Complex-valued Matrix Derivatives: with Applications in Signal Processing and Communications*. Cambridge University Press, 2011.
- [37] J. Du, W. Xu, C. Zhao, and L. Vandendorpe, "Weighted spectral efficiency optimization for hybrid beamforming in multiuser massive MIMO-OFDM systems," *IEEE Trans. Veh. Technol.*, vol. 68, no. 10, pp. 9698–9712, Jul. 2019.
- [38] X. Yu, J. Shen, J. Zhang, and K. B. Letaief, "Alternating minimization algorithms for hybrid precoding in millimeter wave MIMO systems," *IEEE J. Sel. Topics Signal Process.*, vol. 10, no. 3, pp. 485–500, Apr. 2016.
- [39] P.-A. Absil, R. Mahony, and R. Sepulchre, *Optimization Algorithms on Matrix Manifolds*. Princeton University Press, 2009.
- [40] Q. Wu and R. Zhang, "Intelligent reflecting surface enhanced wireless network via joint active and passive beamforming," *IEEE Trans. Wireless Commun.*, vol. 18, no. 11, pp. 5394–5409, Nov. 2019.
- [41] Q. Zhang, S. Jin, K. Wong, H. Zhu, and M. Matthaiou, "Power scaling of uplink massive MIMO systems with arbitrary-rank channel means," *IEEE J. Sel. Topics Signal Process.*, vol. 8, no. 5, pp. 966–981, Oct. 2014.
- [42] R. A. Horn and C. R. Johnson, *Topics in Matrix Analysis*. Cambridge, U.K.: Cambridge Univ. Press, 1994.
- [43] J. D. Kraus and R. J. Marhefka, *Antennas: For All Applications (Third Edition)*. McGraw-Hill, 2008.